

Hole Doping and Structural Transformation in $\text{CsTl}_{1-x}\text{Hg}_x\text{Cl}_3$

Maria Retuerto,^{†,‡} Zhiping Yin,[§] Thomas J. Emge,[†] Peter W. Stephens,[⊥] Man-Rong Li,[†] Tapati Sarkar,^{†,||} Mark C. Croft,[§] Alexander Ignatov,[§] Z. Yuan,[¶] S. J. Zhang,[¶] Changqing Jin,[¶] Robert Paria Sena,[▽] Joke Hadermann,[▽] Gabriel Kotliar,[§] and Martha Greenblatt^{*,†}

[†]Department of Chemistry and Chemical Biology, Rutgers, The State University of New Jersey, 610 Taylor Road, Piscataway, New Jersey 08854, United States

[§]Department of Physics and Astronomy, Rutgers, The State University of New Jersey, 136 Frelinghuysen Road, Piscataway, New Jersey 08854, United States

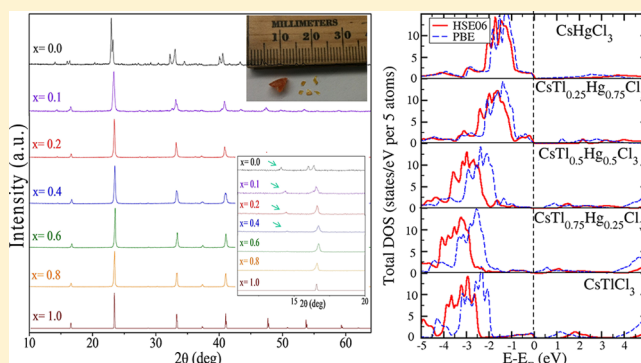
[⊥]Department of Physics & Astronomy, The State University of New York, Stony Brook, New York 11794, United States

[¶]Institute of Physics, Chinese Academy of Sciences, Number 8, Zhongguancun South Street 3, Beijing 100190, China

[▽]EMAT, Department of Physics, University of Antwerp, Groenenborgraan, Antwerp 171 2020, Belgium

S Supporting Information

ABSTRACT: CsTlCl_3 and CsTlF_3 perovskites have been theoretically predicted to be superconductors when properly hole-doped. Both compounds have been previously prepared as pure compounds: CsTlCl_3 in a tetragonal ($I4/m$) and a cubic ($Fm\bar{3}m$) perovskite polymorph and CsTlF_3 as a cubic perovskite ($Fm\bar{3}m$). In this work, substitution of Tl in CsTlCl_3 with Hg is reported, in an attempt to hole-dope the system and induce superconductivity. The whole series $\text{CsTl}_{1-x}\text{Hg}_x\text{Cl}_3$ ($x = 0.0, 0.1, 0.2, 0.4, 0.6,$ and 0.8) was prepared. $\text{CsTl}_{0.9}\text{Hg}_{0.1}\text{Cl}_3$ is tetragonal as the more stable phase of CsTlCl_3 . However, $\text{CsTl}_{0.8}\text{Hg}_{0.2}\text{Cl}_3$ is already cubic with the space group $Fm\bar{3}m$ and with two different positions for Tl^+ and Tl^{3+} . For $x = 0.4$ and 0.5 , solid solutions could not be formed. For $x \geq 0.6$, the samples are primitive cubic perovskites with one crystallographic position for Tl^+ , Tl^{3+} , and Hg^{2+} . All of the samples formed are insulating, and there is no signature of superconductivity. X-ray absorption spectroscopy indicates that all of the samples have a mixed-valence state of Tl^+ and Tl^{3+} . Raman spectroscopy shows the presence of the active $\text{Tl}-\text{Cl}-\text{Tl}$ stretching mode over the whole series and the intensity of the $\text{Tl}-\text{Cl}-\text{Hg}$ mode increases with increasing Hg content. First-principle calculations confirmed that the phases are insulators in their ground state and that Hg is not a good dopant in the search for superconductivity in this system.



INTRODUCTION

Since the discovery of superconductivity in the doped BaBiO_3 compounds, many efforts have been made to find similar superconducting compounds and also to try to understand the mechanism that governs superconductivity in these types of phases.^{1,2} The most relevant characteristic of BaBiO_3 regarding superconductivity is Bi charge disproportionation into low-valent Bi^{3+} ($6s^2$) and high-valent Bi^{5+} ($6s^0$) cations and charge ordering at two different positions for Bi^{3+} and Bi^{5+} , resulting in some deviations from the ideal cubic perovskite structure.³ When BaBiO_3 is hole-doped, as in $\text{Ba}_{1-x}\text{K}_x\text{BiO}_3$, it becomes superconducting with a critical superconducting temperature (T_C) of 34 K for $\text{Ba}_{0.6}\text{K}_{0.4}\text{BiO}_3$.¹ At and below T_C , the structure transforms to the simple cubic perovskite phase, a symmetry that was thought to be necessary for superconductivity.⁴ However, recently in the similar series $\text{BaPb}_{1-x}\text{Bi}_x\text{O}_3$, it was observed that superconductivity was still present even in a noncubic phase.⁵ The observation of superconductivity in

$\text{Ba}_{1-x}\text{K}_x\text{BiO}_3$ or $\text{BaPb}_{1-x}\text{Bi}_x\text{O}_3$ seems to be related to the hole doping of the Bi sites, which suppresses $\text{Bi}^{3+}/\text{Bi}^{5+}$ charge/site ordering and produces metallic behavior and, at low temperatures, superconductivity. These observations suggest that there might be a strong relationship between suppression of the charge ordering and superconductivity.

However, related compounds with similar charge ordering, such as CsAuCl_3 , do not present superconductivity, even at high pressure where structural deviations from cubic symmetry are removed and a metallic state is achieved.^{6–9} Recent models explained superconductivity in doped BaBiO_3 by a correlation-enhanced strong electron–phonon coupling mechanism.² It was shown that electron–phonon coupling is weak in CsAuCl_3 so that superconductivity is not expected.¹⁰ However, other

Special Issue: To Honor the Memory of Prof. John D. Corbett

Received: October 2, 2014

Published: December 9, 2014

calculations predicted that if the Fermi level of CsAuCl₃ could be raised, then superconductivity might be achieved in the family of materials ATlX₃, where A = Rb and Cs and X = Cl, F, and Br, when the compounds are hole-doped.^{10,11} For example, CsTlF₃ and CsTlCl₃ were theoretically predicted to be superconducting upon the optimal ~0.35/formula unit (fu) hole doping and moderate pressures of ~10 and ~2 GPa, with predictions of *T_C* at ~30 and ~20 K, respectively.¹⁰

Recently, we were able to synthesize these two materials, CsTlF₃ and CsTlCl₃, in the perovskite structure predicted to be thermodynamically stable.¹² CsTlF₃ was obtained as a white polycrystalline material with a cubic perovskite structure and Tl⁺ and Tl³⁺ in separate crystallographic positions. CsTlCl₃ was obtained as orange single crystals with two different morphologies: (A) a tetragonal phase, with separate positions for Tl⁺ and Tl³⁺ in alternate octahedra of different sizes; (B) a cubic phase, also with different sites for Tl⁺ versus Tl³⁺. In both polymorphs, there is some site disorder at the Tl⁺ position. Thus, CsTlF₃ and two phases of CsTlCl₃ present Tl⁺/Tl³⁺ charge ordering, which is a potentially good starting point for superconductivity. In addition, electronic band structure calculations showed that the optical band gap of CsTlCl₃ has the required energy if charge ordering is present and that hole doping of this material could lead to superconductivity.¹²

However, all of our efforts to hole-dope CsTlCl₃ by topotactically forming Cs_{1-x}TlCl₃ or by electron doping chemically, e.g., CsTlCl_{3-x}(O,S,N)_x, to achieve superconductivity have not been successful so far. Therefore, analogous to the formation of BaBi_{1-x}Pb_xO₃,¹³ we attempted hole doping by substitution of Hg²⁺ (6s⁰) for the Tl⁺/Tl³⁺ positions and prepared the entire CsTl_{1-x}Hg_xCl₃ (0.0 ≤ *x* ≤ 1.0) series. This was a significant achievement because this class of chlorides is difficult to dope, and any partial doping of CsAuCl₃ has not yet been successful.

EXPERIMENTAL SECTION

A CsTl_{1-x}Hg_xCl₃ (0.0 ≤ *x* ≤ 1.0) series were prepared by mixing stoichiometric quantities of CsCl, TlCl, TlCl₃·*x*H₂O, and HgCl₂ inside a glovebox in order to avoid decomposition of TlCl₃·*x*H₂O into TlCl also because of the hygroscopic character of the starting materials (e.g., the solid TlCl₃·*x*H₂O reagent was deliquescent upon exposure to moist air) and also because of the high toxicity of Tl. The starting materials were mixed, ground, placed in a silica tube, and sealed under vacuum; then they were heated to 600 °C for 12 h, and finally the temperature was decreased at a rate of 5 °C/min, to ambient temperature. The final products were orange intergrown single crystals of ~1–2 mm. Powder X-ray diffraction (PXRD) patterns of the obtained compounds are shown in Figure 1, and single crystals of CsTl_{0.4}Hg_{0.6}Cl₃ are illustrated in the upper inset of Figure 1. The PXRD characterization was carried out on a Bruker D8 X-ray diffractometer (Cu Kα, λ = 1.5418 Å). Synchrotron powder X-ray diffraction (SXRD) data for the Rietveld refinement of the series were collected at room temperature at the National Synchrotron Light Source (NSLS) at Brookhaven National Laboratory using beamline X16C and a wavelength of 0.7001 Å. Rietveld refinements were carried out with TOPAS software.¹⁴ Powder samples were diluted with approximately 90% by weight diamond powder to control absorption in the 1 mm (nominal) Lindemann capillaries, sealed in an inert atmosphere. Single-crystal X-ray diffraction (SCD) data were collected on a Bruker Smart APEX CCD diffractometer with graphite-monochromatized Mo Kα radiation (λ = 0.71073 Å) at 100 K. The data were corrected for Lorenz effects and polarization and for absorption, the latter by a multiscan (SADABS)¹⁵ method. The structure was solved by Patterson methods (SHELXS-86).¹⁶ All atoms were refined using the SHELXL (2013) and JANA2006 programs.¹⁷

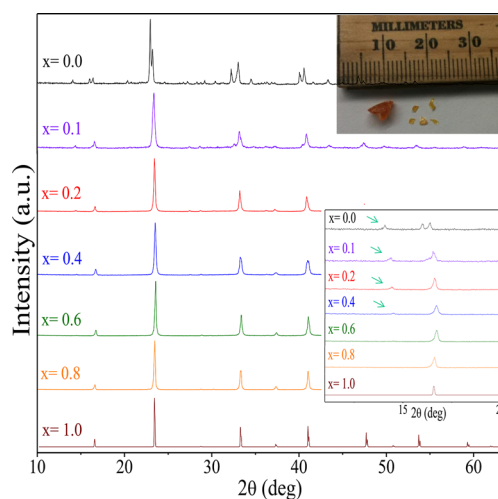


Figure 1. PXRD patterns of CsTl_{1-x}Hg_xCl₃. The upper inset shows the crystals prepared. The lower inset shows a zoom of the low-angle area to highlight the superstructure peaks.

X-ray absorption spectroscopy (XAS) measurements were made in both fluorescence and transmission modes on beamline X-19A at the NSLS with a Si(111) double-crystal monochromator.^{18,19} The Tl L₃-edge measurements were made in both transmission and fluorescence modes with a simultaneous run of the Tl₂O₃ standard for energy calibration. The low energy of the Cl K-edge measurements were possible because of the 100 μm Be beamline window and a specially designed He atmosphere fluorescence mode chamber. Energy calibration in the Cl K-edge measurements was made by frequent running of the same standard in the sequence of scans. The data were processed with standard linear pre- and postedge background subtraction. The absorption coefficient (μ) was normalized to 1.0 over an average energy region well above the edge. The Raman spectra of this CsTl_{1-x}Hg_xCl₃ series were recorded with the Renishaw Micro-Raman Spectroscopy System with a laser wavelength of 532 nm and an output power of 100 mW.

RESULTS AND DISCUSSION

Elemental analyses were carried out by inductively coupled plasma (ICP) mass spectrometry to determine the ratio of Tl and Hg in each sample. The compositions determined for several crystals were 80(1)% Tl/20(1)% Hg for nominal CsTl_{0.8}Hg_{0.2}Cl₃, 61(1)% Tl/39(1)% Hg for nominal CsTl_{0.6}Hg_{0.4}Cl₃, 46(1)% Tl/54(1)% Hg for nominal CsTl_{0.4}Hg_{0.26}Cl₃, and 23(1)% Tl/77(1)% Hg for nominal CsTl_{0.2}Hg_{0.8}Cl₃. In all cases, Cs atoms are stoichiometric within the error range of the respective formula given above. Because of the close agreement of the chemically analyzed compositions with nominal compositions, the nominal compositions are employed to designate the compositions of the samples. The X-ray fluorescence (XRF) analyses of the above samples were consistent with the respective ICP results.

Crystal Structure. Figure 1 shows the PXRD patterns of the CsTl_{1-x}Hg_xCl₃ (*x* = 0.0, 0.1, 0.2, 0.4, 0.6, 0.8, and 1.0) series. For pure CsTlCl₃, we have previously reported two phases: a body-centered tetragonal phase (*I4/m*) and a relatively less stable cubic phase (*Fm* $\bar{3}$ *m*).¹² A similar tetragonal structure was observed for the *x* = 0.1 compound. The PXRD pattern of the tetragonal phase contains the “split peak” features consistent with the tetragonal phase (*I4/m*) found for *x* = 0.0, namely, *a*' ≈ *b*' ≈ 17 Å and *c*' ≈ 11 Å for the *a*' = 5^{1/2}*a* and *c*' = *c* superlattice,¹² with respect to the known *a* ≈ *b* ≈ 7 Å and *c* ≈ 11 Å of the tetragonal (*I4/mmm*) CsMCl₃ (M = Au and Ag)

phases.^{20,21} The formation of this superlattice is expected because of the lone pair effect of the Tl⁺ (6s²) cation in this tetragonal site, which allows for distortion in the structure and tilting of the TiO₆ octahedral with respect to an undistorted cubic sublattice. For $x \geq 0.2$, the PXRD patterns (Figure 1) indicate that the structures have cubic symmetry. Thus, the substitution of small amounts of Hg for Tl in CsTl_{1-x}Hg_xCl₃ is apparently sufficient to stabilize a cubic perovskite instead of a lower-symmetry tetragonal phase.

The lower inset of Figure 1 shows the 10° < 2θ < 20° region of the PXRD patterns. In a comparison of the PXRD data of the cubic samples ($x = 0.2, 0.4, 0.6, 0.8, \text{ and } 1.0$), it was observed that an F-centered cubic reflection exists at 2θ = 14° only for $x \leq 0.4$. This observed peak and the less intense peaks expected at 2θ = 27° and 36° are the result of inequivalent B sites for Tl in this perovskite at (0, 0, 0) and (1/2, 1/2, 1/2), as found for the *Fm* $\bar{3}m$ phase of Cs₂Au⁺Au³⁺Cl₆, namely, Au³⁺ at (0, 0, 0) and Au⁺ at (1/2, 1/2, 1/2).²² We have previously observed the same F centering in the cubic phase of CsTlCl₃, where weak peaks at 14° and 27° are explained by the presence of Tl⁺ and Tl³⁺ in two different crystallographic sites. This should be expected because Tl⁺ and Tl³⁺ have very different ionic sizes (1.5 and 0.885 Å, respectively).²³ Also, the lone-pair effect of Tl⁺ is expected to create a very different environment for its Tl⁺Cl₆ octahedra compared to Tl³⁺Cl₆.

For $x \geq 0.6$, the lattice is primitive in a cubic perovskite model (CaTiO₃ structural type, *Pm* $\bar{3}m$) with one B site for all Tl or Hg atoms. This finding could be of great significance because, if the two different positions for Tl⁺ and Tl³⁺ no longer exist, then we may have been able to dope the cubic CsTlCl₃ phase and prepare for the first time a compound with single-valent Tl²⁺ at one position. This would be a good starting point in the search for superconductivity in this type of material, in the manner predicted by Yin and Kotliar¹⁰ and experimentally observed in K-doped BaBiO₃.¹ However, it is more likely that both Tl⁺ and Tl³⁺ occupy the single B position or that an overabundance of Hg²⁺ in one site masks the true positions of Tl⁺ and Tl³⁺ wherever they are. The results of Raman spectroscopy helped us to confirm the presence of Tl⁺ and Tl³⁺ rather than the intermediate Tl²⁺ (see below).

We were able to use the SCD results to find precise models of the primitive and F-centered phases and to determine the extent of atomic site disorder. We collected data on different crystals of the same batches of $x = 0.2, 0.6, \text{ and } 0.8$ for CsTl_{1-x}Hg_xCl₃. We do not report SCD results here for the $x = 0.4$ material because the SXRD data strongly indicated that it was most likely not a single phase (see below).

Consistent with the PXRD result, the SCD data of CsTl_{0.8}Hg_{0.2}Cl₃ ($x = 0.2$) agree best with the *Fm* $\bar{3}m$ double perovskite model, very similar to the one we previously reported for cubic CsTlCl₃ and to that reported for CsAuCl₃. In our model for the $x = 0.2$ phase, the Cs site at 8c (1/4, 1/4, 1/4) has a slight disorder, as evidenced by small, but significant (about 3 e/Å³), residuals in the difference electron density map, but refinement of any off-site atom failed because of large correlation coefficients, as expected from the small distance (about 0.5 Å) to the 8c site. The Tl site at 4a (0, 0, 0) was ordered and fully occupied and was assigned as Tl only. The Hg(2A)/Tl(2B) site at 4b (1/2, 0, 0) was noticeably split, with the majority of the electron density at the 24e position ($x, 0, 0$) with $x = 0.5721(10)$ and much less electron density at the 4b position (1/2, 0, 0). This overall site was modeled with Hg at the 4b site and Tl at the 24e site and initially refined to 14 and

86% occupancy, respectively. For the final cycles of refinement, the 4b and 24e sites were given different isotropic displacement parameters but fixed at 1/6 and 5/6 occupancies, respectively, in order to (A) agree with the Cl atom site disorder of 5:1 (see below), (B) be consistent with 1 out of 6 Tl–Cl bonds being unrealistic (<2 Å) and ignored here, resulting in 4- or 5-coordinate Tl, and (C) yield the overall stoichiometry CsTl_{0.8}Hg_{0.2}Cl₃ ($x = 0.2$). The correlation matrix element for $U^{11}[\text{Hg}(2A)]/U^{11}[\text{Tl}(2B)]$ was 0.516 (program *SHELXL*, version 2014_3). The Cl(1A) site at 24e ($x, 0, 0$) with $x = 0.2413(9)$ was ordered but not fully occupied, and a second Cl(1B) site was found at 48h ($x, x, 0$) with $x = 0.165(4)$, at a substantial distance (2 Å) away. After restrained refinement, it was found that the occupancies of Cl(1A) and Cl(1B) were approximately 5/6 and 1/6 and were subsequently set equal to these values, respectively, and the same isotropic displacement parameter was refined for Cl(1A) and Cl(1B). The final atomic coordinates and anisotropic displacement parameters are listed in Table 1, and the bond distances and angles are given in Table 2. The Tl(1)–Cl(1A) distance of 2.608(10) Å is significantly shorter than the Hg(2A)–Cl(1A) distance of 2.795(10) Å, consistent with Tl³⁺ at the Tl(1) site and Hg²⁺ at

Table 1. Crystal Data and Atomic Parameters for CsTl_{1-x}Hg_xCl₃ at 100 K for $x = 0.2, 0.6, \text{ and } 0.8^a$

<i>Fm</i> $\bar{3}m$	$x = 0.2$	<i>Pm</i> $\bar{3}m$	$x = 0.6$	$x = 0.8$
<i>a</i> /Å	10.804(2)	<i>a</i> /Å	5.3739(14)	5.3750(11)
<i>V</i> /Å ³	1261.3(8)	<i>V</i> /Å ³	155.19(12)	155.29(6)
Cs(1) 8c (1/4, 1/4, 1/4)		Cs 1a (0, 0, 0)		
<i>U</i> ₁₁ /Å ²	0.0855(16)	<i>U</i> ₁₁ /Å ²	0.0472(9)	0.0371(41)
occupancy	1.000	occupancy	1.000	1.000
Tl/Hg(1) 4a (0, 0, 0)		Tl/Hg(1A) 1b (1/2, 1/2, 1/2)		
<i>U</i> ₁₁ /Å ²	0.0286(6)	<i>U</i> ₁₁ /Å ²	0.0216(5)	0.0160(3)
occupancy	1.000	occupancy	0.880(8)	0.947(5)
Hg(2A) 4b (1/2, 0, 0)		Tl/Hg(1B) 6f (<i>x</i> , 1/2, 1/2)		
<i>U</i> ₁₁ /Å ²	0.0028(16)	<i>x</i>	0.346(5)	0.352(7)
occupancy	0.167	<i>U</i> ₁₁ /Å ²	0.0216(5)	0.0160(3)
		occupancy	0.120(8)	0.053(5)
Tl(2B) 24b (<i>x</i> , 0, 0)				
<i>x</i>	0.5720(10)			
<i>U</i> _{iso} /Å ²	0.066(3)			
occupancy	0.833			
Cl(1A) 4e (<i>x</i> , 0, 0)		Cl 3c (0, 1/2, 1/2)		
<i>x</i>	0.2413(9)	<i>U</i> ₁₁ /Å ²	0.088(7)	0.099(5)
<i>U</i> ₁₁ /Å ²	0.056(5)	<i>U</i> ₁₂ /Å ²	0.065(4)	0.069(2)
<i>U</i> ₁₂ /Å ²	0.059(3)	occupancy	1.000	1.000
occupancy	0.833			
Cl(1B) 48h (<i>y</i> , <i>y</i> , 0)				
<i>y</i>	0.164(5)			
<i>U</i> ₁₁ /Å ²	0.056(5)			
<i>U</i> ₁₂ /Å ²	0.059(3)			
occupancy	0.167			
R1	0.0513	R1	0.0337	0.0246
wR2	0.1142	wR2	0.0663	0.0637

^aThe anisotropic displacement factor exponent takes the form $-2\pi^2[h^2a^{*2}U_{11} + \dots + 2hka^*b^*U_{12}]$, with U_{ij} in square angstroms.

Table 2. Main Interatomic Distances (Å) for the CsTl_{1-x}Hg_xCl₃ Series at 100 K

<i>Fm</i> $\bar{3}$ <i>m</i>	<i>x</i> = 0.2	<i>Pm</i> $\bar{3}$ <i>m</i>	<i>x</i> = 0.6	<i>x</i> = 0.8
Cs(1A)–Cl(1A) (×12)	3.821(1)	Cs–Cl (×12)	3.800(1)	3.801(1)
Cs(1A)–Cl(1B) (×6)	3.01(3)			
Tl/Hg(1)–Cl(1A) (×6)	2.61(1)	Tl/Hg(1A)–Cl (×6)	2.687(1)	2.688(1)
Tl/Hg(1)–Cl(1B) (×6)	2.50(7)	Tl/Hg(1B)–Cl (×4)	2.812(9)	2.802(11)
		Tl/Hg(1B)–Cl (×1)	3.515(9)	3.483(11)
Tl/Hg(2A)–Cl(1A) (×6)	2.79(1)			
Tl/Hg(2B)–Cl(1A) (×4)	2.90(1)			

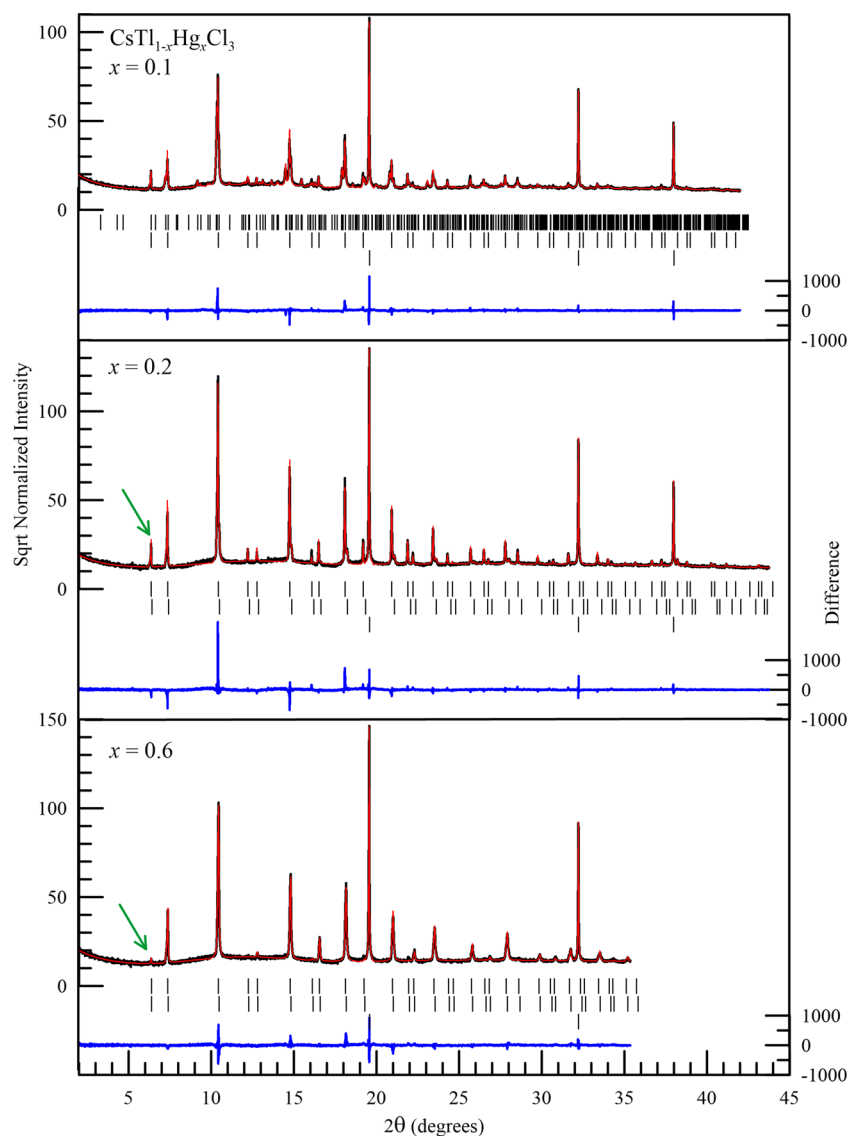


Figure 2. SPXD patterns of CsTl_{1-x}Hg_xCl₃ for *x* = 0.1, 0.2, and 0.4. The black trace is raw data, red is the Rietveld refinement, and blue is the difference (linear scale on the right). In the top panel, the dense row of tick marks are allowed peak positions of the tetragonal phase, the middle row is the cubic phase, and the bottom row is the diamond powder used for diluent and internal standard. Green arrows in the *x* = 0.2 and 0.6 panels indicate the (111) peak present in the doubled *Fm* $\bar{3}$ *m* phase, which would be absent for the *Pm* $\bar{3}$ *m* primitive cell.

the Hg(2A) site, although Hg cannot be distinguished from Tl by this X-ray experiment and is only assigned here. Both distances are smaller than expected by Shannon,²³ as happens in other similar phases, such as CsAuCl₃ or ClAgCl₃.^{21,22} Also, it has been found that the off-site residual density was more appropriately modeled by site disorder (here, in program *SHELXL*, which yields ranges of bond geometries as in Table 2) rather than by the use of anharmonic displacement

parameters, such as those available in refinement program *JANA2006* (which yields average bond geometries).

Rietveld fits of the SXRD results, shown in Figure 2, support this interpretation but show that all of the powder samples have two coexisting phases. The *x* = 0.1 sample is a 50:50 mixture of the tetragonal phase with *a* = 17.1498(3) Å and *c* = 11.0823(3) Å and a cubic (*Fm* $\bar{3}$ *m*) phase with *a* = 10.9042(3) Å. The *x* = 0.2 sample is 90% of the *Fm* $\bar{3}$ *m* phase with *a* = 10.9019(3) Å

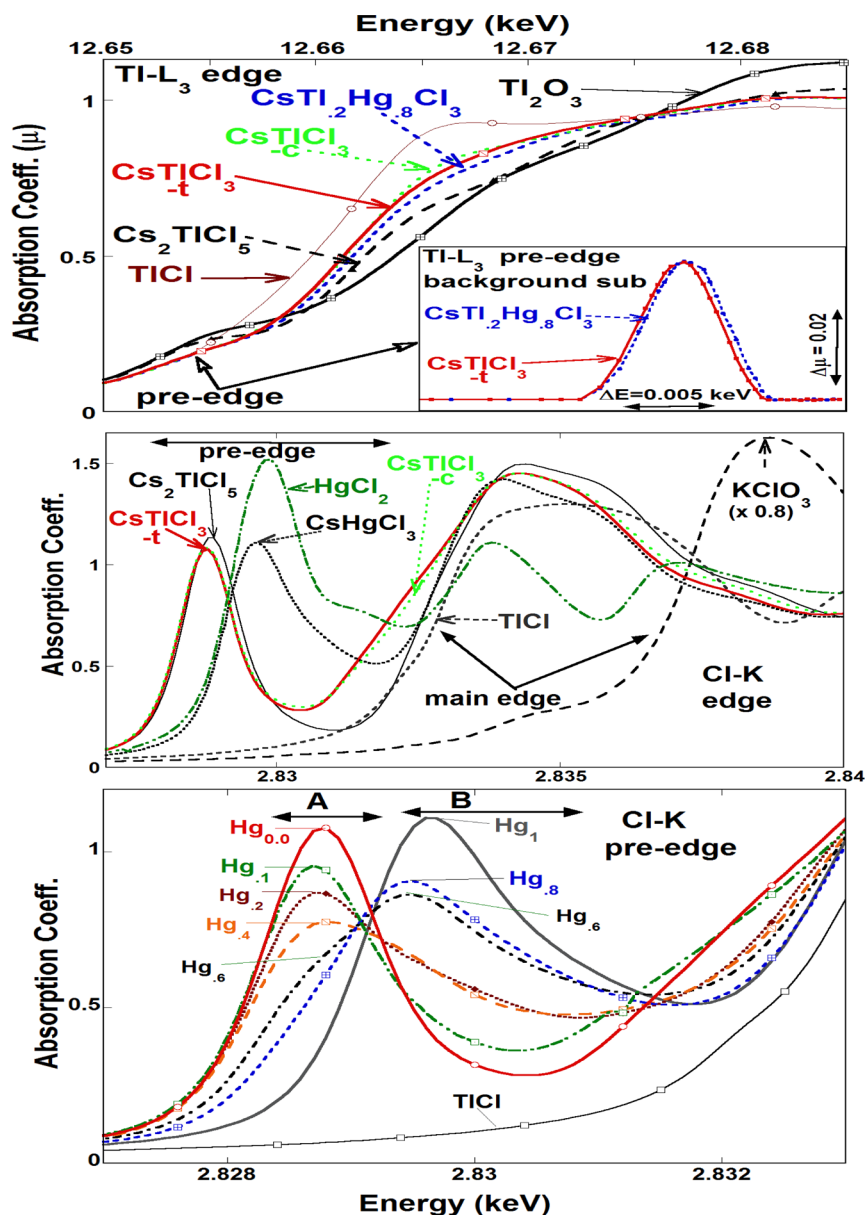


Figure 3. (a) Tl L_3 -edges of CsTlCl_3 , $\text{CsTl}_{0.2}\text{Hg}_{0.8}\text{Cl}_3$, Tl^{3+} standards (Tl_2O_3 and Cs_2TlCl_5), and Tl^+ standard TlCl . Inset: expanded view of the Tl L_3 -pre-edge region with a feature related to empty 6s final states. The background was subtracted. (b) Cl K-edges of CsTlCl_3 -t, CsTlCl_3 -c, CsHgCl_3 , and standards. Note that the KClO_3 spectrum has been multiplied by a factor of 0.8 to facilitate a comparison on a similar vertical scale. The prominent, pre-edge, s-hole related features of all compounds (except s^2 of TlCl) are noted. (c) Comparison of Cl K-preedges of $\text{CsTl}_{1-x}\text{Hg}_x\text{Cl}_3$ compounds. Note the systematic transfer of the spectral weight between A and B features with increasing Hg content.

and 10% with $a = 10.8206(3)$ Å. The $x = 0.4$ sample (not shown) is a roughly 50:50 mixture of the $Fm\bar{3}m$ phases with $a = 10.9026(3)$ and $10.8616(3)$ Å; interestingly, the odd-order peaks are much stronger in the phase with the larger lattice parameter, which is essentially identical with the lattice parameter of the majority phase of the $x = 0.2$ sample. The split 4b site model described above is required to explain the intensity of the odd-order peaks; differences in the valence or occupancy of the two Tl sites alone cannot account for the measured SXRD patterns.

The SCD data of different crystals of $x = 0.6$ and 0.8 ($\text{CsTl}_{1-x}\text{Hg}_x\text{Cl}_3$) have the well-known primitive cubic perovskite model $Pm\bar{3}m$, with Tl or Hg atoms located at or near the 1b ($1/2, 1/2, 1/2$) site and Cs atoms at the 1a (0, 0, 0) sites. The Tl/Hg(1A) site at 1b ($1/2, 1/2, 1/2$) was disordered, with partial

occupancy at 1b and a sextet of positions about the 1b site modeled by Tl/Hg(1B) at 6f ($x, 1/2, 1/2$) with $x = 0.35$ and occupancies of 0.02 or less for both $\text{CsTl}_{0.4}\text{Hg}_{0.6}\text{Cl}_3$ and $\text{CsTl}_{0.2}\text{Hg}_{0.8}\text{Cl}_3$. In the case of $\text{CsTl}_{0.4}\text{Hg}_{0.6}\text{Cl}_3$, the occupancy at 1b was refined to a slightly larger value than that of $\text{CsTl}_{0.2}\text{Hg}_{0.8}\text{Cl}_3$ (see Table 2). The Cl site in these two $Pm\bar{3}m$ structures appears to be ordered and fully occupied at a single site 3c (0, $1/2, 1/2$). The Tl/Hg–Cl distance for either $Pm\bar{3}m$ structure was about 2.69 Å and between those for the $Fm\bar{3}m$ structure. The coordination geometries of $x = 0.6$ and 0.8 are very similar to each other and do not appear to correlate with the Hg/Tl ratio in any way. The final atomic coordinates and anisotropic displacement parameters are listed in Table 1 and the main Tl/Hg(1A) and minor Tl/Hg(1B) site bond distances and angles in Table 2. As shown in Table 1, the cell

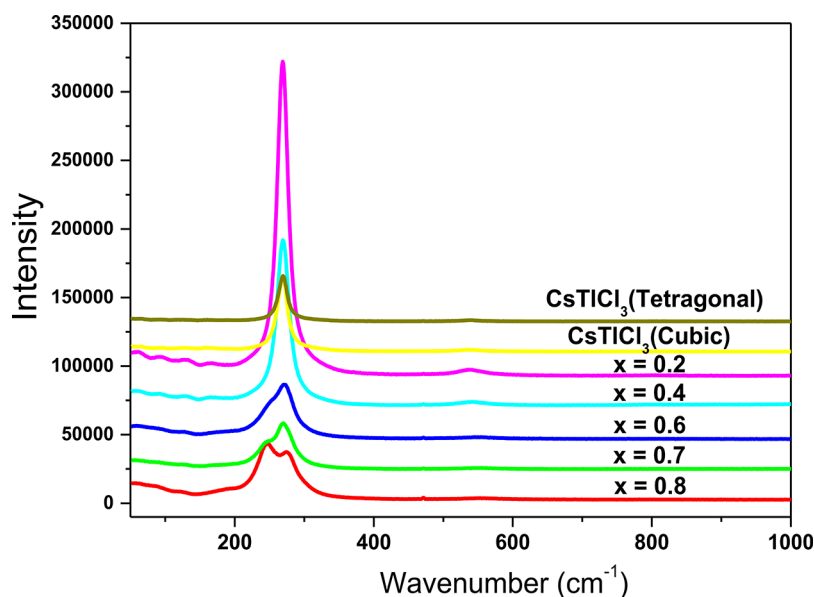


Figure 4. Evolution of the Raman spectra of $\text{CsTl}_{1-x}\text{Hg}_x\text{Cl}_3$.

parameters decrease as the content of Hg increased, correlating well with the values of the ionic radii for Tl^+ ($r^{\text{VI}} = 1.5 \text{ \AA}$) and Tl^{3+} ($r^{\text{VI}} = 0.885 \text{ \AA}$), for an average of 1.19 \AA for Tl, and for Hg^{2+} ($r^{\text{VI}} = 1.02 \text{ \AA}$).²³

Attempts to prepare $\text{CsTl}_{0.5}\text{Hg}_{0.5}\text{Cl}_3$ were not successful, which indicates that it may not be possible to form the full range of solid solutions in $\text{CsTl}_{1-x}\text{Hg}_x\text{Cl}_3$. Also, these samples were prepared as single crystals from self-flux, and for $\text{CsTl}_{0.6}\text{Hg}_{0.4}\text{Cl}_3$, different compositions are formed at different locations inside the quartz tube; e.g., the crystals grown on the walls of the tube have cell data similar to those of $\text{CsTl}_{0.4}\text{Hg}_{0.6}\text{Cl}_3$, while the ones grown in the middle of the flux have cell data similar to those of $\text{CsTl}_{0.8}\text{Hg}_{0.2}\text{Cl}_3$.

Figure 2c shows the SXRD data of $x = 0.6$ ($\text{CsTl}_{0.4}\text{Hg}_{0.6}\text{Cl}_3$). Contrary to the PXRD and SCD results, the synchrotron data show very small F-centering peaks at 6.38° , 16.13° , and 19.25° . These are too weak to support the split-site model but could arise from valence or vacancy ordering on the two Tl sites. The discrepancy could arise because the harvest region of this sample was close to the area where the solid solution was not formed and multiple phases may form. Doubled cell parameters of $10.856(5)$ and $10.884(5) \text{ \AA}$ were observed in that powder. To confirm that the $Pm\bar{3}m$ crystals contain Tl and Hg and are not just pure CsHgCl_3 , we carried out XRF and observed $36.2(2)\%$ Tl/ $63.8(2)\%$ Hg. The presence of Tl was also indicated by the orange color, compared to the white/colorless crystals of pure CsHgCl_3 .

Crystals of the compound with $x = 0.8$ ($\text{CsTl}_{0.2}\text{Hg}_{0.8}\text{Cl}_3$) were orange in color but visibly lighter color crystals, as may be expected because of the relative reduction of Tl color centers. The SXRD of this compound refined well in the simple perovskite model $Pm\bar{3}m$, as we previously observed by SCD, and we used that model for the refinement, which gave a refined cell parameter of $5.4161(1) \text{ \AA}$.

We measured the magnetic properties of all of the members of the series between 5 and 300 K, but none were magnetically interesting and the signals are so low that we cannot trust the measurements and separate them from the background or the signal of the plastic sample holder; thus, the samples are not magnetic.

XAS. We performed XAS to observe whether there is a change in the Tl oxidation state as the content of Hg increases and also to see whether there is any change in the shape of the curves indicating an evolution from mixed $\text{Tl}^+/\text{Tl}^{3+}$ state to a single Tl^{2+} state. Tl usually presents Tl^+ and Tl^{3+} valence states: Tl^{3+} involves two $6s$ orbital holes and Tl^+ ($6s^2$) none. The Tl L_3 -edge XAS signature of a Tl^+ to Tl^{3+} change is a chemical shift of the main edge to higher energy and the appearance of a shoulder preedge feature due to transitions into the empty $6s$ hole states.¹² These same signatures are observed in the Bi L_3 -edge from Bi^{3+} to Bi^{5+} .^{24–26} In Figure 3a, the Tl L_3 -edge spectra for the perovskite compounds CsTlCl_3 (-c, cubic; -t, tetragonal) and $\text{CsTl}_{0.2}\text{Hg}_{0.8}\text{Cl}_3$ are compared to those of Tl^+ and Tl^{3+} standards, with the preedge energy region being noted. The energy where the absorption coefficient first rises to the $\mu \sim 0.5$ value can be used to compare the nominal chemical shift of such spectra. The chemical shift of the CsTlCl_3 structure is clearly intermediate between those of the Tl^+ and Tl^{3+} standards, supporting its intermediate valence.¹² Also, the cubic and tetragonal forms have nearly identical spectra and will therefore not be discussed separately hereafter in the XAS discussions. The chemical shift of $\text{CsTl}_{0.2}\text{Hg}_{0.8}\text{Cl}_3$ appears displaced somewhat to higher energy but still falls in the intermediate valence range. The Tl L_3 -edges of various other x compositions in the $\text{CsTl}_{1-x}\text{Hg}_x\text{Cl}_3$ series (not shown) have chemical shifts falling (with scatter) within these two extremes without manifesting a definitive systematic trend. Thus, the retention of valence mixing in this series was indicated. Focusing on the preedge region of the spectra in Figure 3a, one notes pronounced preedge shoulder features consistent with the presence of two $6s$ orbital holes ($6s^0$ configuration) in the Tl^{3+} compounds, Tl_2O_3 and Cs_2TlCl_5 . In contrast, the Tl^+Cl spectrum exhibits a monotonic concave upward curvature over the entire pre edge region, consistent with the absence of any $6s$ hole states ($6s^2$ configuration).

The Cl K-near-edge is dominated by dipole-allowed $1s$ -to- $2p$ transitions. The Cl K-near-edges for a series of Cl compounds is shown in Figure 3b. The simple structureless main-edge rise and broad peak for Cl^- in TlCl is typical for the ionic bonding and filled $2p$ orbitals in these materials. Cl^{5+} in the KClO_3

spectrum, on the other hand, displays an intense “white line” feature due to transitions into the now empty 2p orbitals, along with a very substantial chemical shift of the main edge to higher energy. The most striking structure in the other spectra in Figure 3b is the extremely intense pre-edge features shifted well below the main-edge rise. In transition-metal compounds, such Cl K-pre-edge features, associated with the metal d-orbital states hybridized with the ligand Cl p states, are common. Indeed, the d-orbital subsplitting, bandwidths, and energies have been studied with Cl K-edge XAS.^{27,28} In the Tl compounds considered here, such pre-edge features are associated with transitions into Cl 2p states hybridized with Tl 6s hole states.¹² Note that, in the filled 6s² TlCl spectrum, no hint of the pre-edge feature was present. In the Cl K-edges of the CsHgCl₃ perovskite and the HgCl₂ standard, the prominent 6s-hole pre-edge feature was shifted less far below the main edge because of the smaller binding energy of the Hg 6s states relative to those of Tl 6s, which see a larger effective core charge. The pre-edge of Tl³⁺ in Cs₂TlCl₅ in Figure 3b manifests the pre-edge feature with the highest spectral intensity and the simplest structure. The CsTlCl₃-t and -c pre-edge features are reproducibly, albeit slightly, shifted to lower energy and exhibit a slightly lower spectral intensity in the pre-edge peak. Both spectra, however, evidence excess intensity and an additional substructure between the peak and main-edge rise. See, for example, the less deep minima in the intensity in the pre-edge region and the bulge most prominently observed on the rising edge of the CsTlCl₃-t spectrum. Although detailed electronic structure calculations will be required to clarify these spectral features, there is a definite disparity from pure Tl³⁺ standard behavior. In Figure 3c, the evolution of the pre-edge feature region as a function of Hg substitution in the CsTl_{1-x}Hg_xCl₃ series is shown. The systematic transfer of the intensity from the Tl 6s, A feature to the Hg 6s, B feature with increasing *x* is dramatically apparent. Indeed, this appears to be nearly a textbook example of the spectral evolution expected with the *x* variation in the fraction of the A versus B transition channels.

Raman Spectroscopy. Figure 4 shows the Raman data of CsTl_{1-x}Hg_xCl₃. The Tl–Cl–Tl and Hg–Cl–Hg bond phonon frequencies are expected to be within a few cm⁻¹ of each other and situated around 270 cm⁻¹. In the case of monoclinic CsHgCl₃ this frequency was known to be the Cl-breathing mode for Hg–Cl–Hg.²⁹ When CsTl_{1-x}Hg_xCl₃ is in a cubic phase, this Hg–Cl–Hg breathing mode is not Raman-active because of symmetry, and neither will be Tl²⁺–Cl–Tl²⁺ mode, so the active mode will be the nonsymmetrical Tl⁺–Cl–Tl³⁺. Because these frequencies are indeed observed in all of the members of the CsTl_{1-x}Hg_xCl₃ series, we most likely have the Tl⁺–Cl–Tl³⁺ modes active here.

Another peak appeared around 240 cm⁻¹ which should be related to the Hg–Cl–Tl bond with a calculated phonon frequency of 230 cm⁻¹. This frequency can be Raman active for any crystal symmetry, corresponds to Hg–Cl–Tl³⁺ or Hg–Cl–Tl⁺, and can be computed by assuming a *Fm-3m* structure with Tl at (0 0 0) and Hg at (1/2 1/2 1/2). This peak increased as the content of Hg increased and was very noticeable for CsTl_{0.2}Hg_{0.8}Cl₃, where there are more Tl–Cl–Hg interactions than Tl–Cl–Tl.

First-Principle Calculations. To gain further insights into how Hg doping changes the crystal and electronic structures of this class of materials, we carried out first-principles density functional theory (DFT) calculations with both the generalized gradient approximation (the PBE version)³⁰ and the screened

hybrid (the HSE06 version)³¹ exchange-correlation functional, as implemented in the VASP code.³² First of all, we show in Figure 5 the band structures of the parent compounds CsTlCl₃

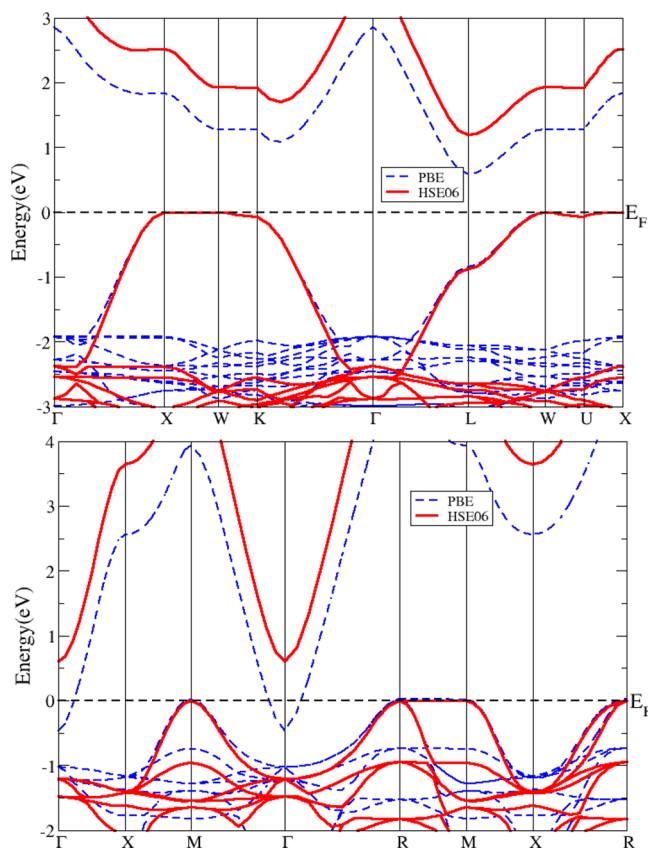


Figure 5. Band structure of (a, top) face-centered-cubic CsTlCl₃ and (b, bottom) simple cubic CsHgCl₃ using DFT-PBE and DFT-HSE06.

and CsHgCl₃. As reported in ref12, the face-centered-cubic parent compound CsTlCl₃ is an insulator with an indirect band gap of 1.2 eV and an optical gap of 1.9 eV within the HSE06 approach (see Figure 5a). The band gap is between the occupied Tl⁺ 6s band and the empty Tl³⁺ 6s band. Using the experimental simple cubic perovskite structure with lattice constant *a* = 5.41 Å for CsHgCl₃, DFT-HSE06 calculations predict a 0.6 eV indirect band gap and a 1.8 eV optical gap, which is between the occupied Cl 3p bands and the empty Hg 6s band (see Figure 5b). This prediction is consistent with the experimental observation of insulating the behavior of CsHgCl₃. In contrast, DFT-PBE calculations predict that CsHgCl₃ is metallic (but is on the border of a metal–insulator transition), which is inconsistent with experiment. We note, however, that the simple cubic perovskite structure of CsHgCl₃ is unstable against the Jahn–Teller distortion of HgCl₆ octahedra in both the DFT-PBE and DFT-HSE06 approaches, which predict that the planar and apical Cl atoms are displaced from the simple cubic perovskite positions by about 0.1 and 0.2 Å, respectively. We further note that second-order Jahn–Teller (SOJT) distortions could occur in d¹⁰ ions as Hg²⁺, when the symmetry of the empty *ns* orbitals have the appropriate symmetry to mix with certain (*n* – 1)d orbitals, but confirming the SOJT effect will require a more careful study of the pure CsHgCl₃ phase.

Noting that heavily Hg-doped CsTlCl₃ has nearly simple cubic structure experimentally, we study a hypothetical cubic

compound $\text{Cs}_2\text{TlHgCl}_6$ to investigate the effect of Hg doping on electron–phonon coupling. We use a $Fm\bar{3}m$ perovskite structure with Cs occupying $(\frac{1}{4}, \frac{1}{4}, \frac{1}{4})$, Tl $(0, 0, 0)$, Hg $(\frac{1}{2}, \frac{1}{2}, \frac{1}{2})$ and Cl $(x, 0, 0)$ and equivalent positions. Structure optimizations using HSE06 and PBE both give a value of $x \sim 0.255$ at equilibrium structure. The band structures at equilibrium structure are computed using both HSE06 and PBE and shown in Figure 6a. Both HSE06 and PBE predict a

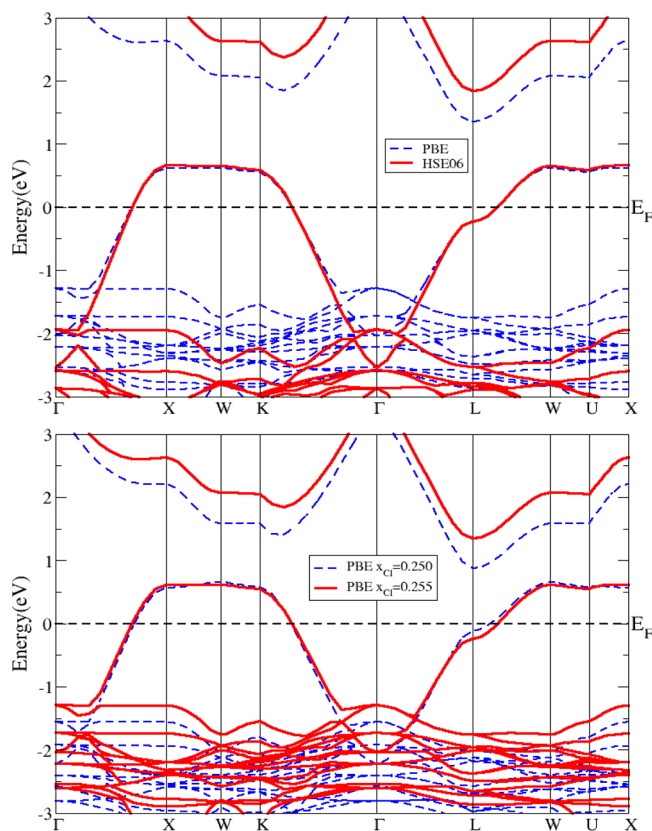


Figure 6. Band structure of the hypothetical face-centered-cubic $\text{Cs}_2\text{TlHgCl}_6$ using DFT-PBE and/or DFT-HSE06 at (a) equilibrium structure ($x = 0.255$) and (b) at $x = 0.255$ and 0.250 .

metallic band structure with almost the same dispersion around the Fermi level. The separation of the Tl 6s band crossing the Fermi level and the Hg 6s band above the Tl 6s band is about 0.5 eV larger in the HSE06 band structure. In Figure 6b, we show the PBE band structure at the equilibrium structure $x = 0.255$ and at $x = 0.250$, where the Cl atoms are displaced from the equilibrium positions. These displacements of the Cl atoms lead to only a small shift of the Tl 6s band, which crosses the Fermi level. The largest shift is along the L–W high-symmetry line with only about 1.5 eV/Å for the reduced electron–phonon matrix element, a drastic reduction from the value of about 4.9 eV/Å for the parent CsTiCl_3 compound.¹⁰ Because electron–phonon coupling is proportional to the square of the reduced electron–phonon matrix element,² therefore Hg doping rapidly suppresses electron–phonon coupling of the Cl breathing mode. Hence, Hg is a bad dopant for inducing superconductivity. The underlying reason is that Hg doping breaks the symmetry of the Tl–Cl–Tl bonds, leading to a different band structure around the Fermi level. In order to keep the Tl–Cl–Tl bond intact, doping of the Cs site is a

better choice in order to metalize the CsTiCl_3 parent compound.

The metallicity of the hypothetical $\text{Cs}_2\text{TlHgCl}_6$ compound is, however, inconsistent with experimental observations that all of the Hg-doped CsTiCl_3 including CsHgCl_3 are insulating. It is possible that the actual structures of the doped compounds have different local distortions from what is assumed above. To investigate other possible local distortions, we construct a $2 \times 2 \times 2$ supercell of the simple cubic perovskite unit cell to study the partially doped $\text{Cs}(\text{Tl,Hg})\text{Cl}_3$ materials and assume periodic conditions. The supercell contains 8 Cs atoms, 24 Cl atoms, and a total number of 8 Tl and Hg atoms. We vary the number of Hg atoms to study different Hg-doping levels. First of all, an odd number of Hg atoms (1, 3, 5, or 7) results in an odd number of total electrons in the supercell, which in the band theory results in a metallic electronic structure. This is a limitation of the relatively small size of the supercell but does not suggest that the system is metallic at these doping levels (12.5%, 37.5%, 62.5%, and 87.5%). Therefore, we carried out detailed studies for an even number of Hg atoms (2, 4, or 6), which corresponds to 25%, 50%, and 75% Hg doping.

We start with 25% Hg doping with an initial structure of CsTiCl_3 in the cubic phase; i.e., the Cl atoms are displaced from the simple cubic perovskite positions. We have also slightly and randomly displaced all of the atoms from the $Fm\bar{3}m$ cubic perovskite positions in all three directions so that the structure relaxation is not constrained to a particular space group. Because the structure relaxation can only find a local minimum and not a global minimum, different initial configurations of the Hg atoms could be trapped in structures with different local minimal total energy. Therefore, all of the different initial configurations have to be considered. Out of the eight positions of the Tl/Hg atoms, $(0, 0, 0)$, $(\frac{1}{2}, 0, 0)$, $(0, \frac{1}{2}, 0)$, $(0, 0, \frac{1}{2})$, $(\frac{1}{2}, \frac{1}{2}, 0)$, $(\frac{1}{2}, 0, \frac{1}{2})$, $(0, \frac{1}{2}, \frac{1}{2})$, and $(\frac{1}{2}, \frac{1}{2}, \frac{1}{2})$, there are only three different initial configurations for the two Hg atoms: they are at (1) $(0, 0, 0)$ and $(0, \frac{1}{2}, 0)$, (2) $(0, 0, 0)$ and $(\frac{1}{2}, \frac{1}{2}, 0)$, and (3) $(0, 0, 0)$ and $(\frac{1}{2}, \frac{1}{2}, \frac{1}{2})$ within the supercell. All other configurations are equivalent to one of these three configurations. With these initial configurations, we fully relax the atomic positions using the PBE functional. Note that both PBE and HSE06 predicted reasonable structure for CsTiCl_3 .¹² Although HSE06 is slightly better than the PBE for the structure relaxation of CsTiCl_3 ,¹² it is very computationally demanding. Therefore, we use only the PBE functional for structure relaxation in this study. After relaxation, the force acting on each atom in each direction is less than 0.1 meV/Å. Of the three configurations after relaxation, the first one with the shortest Hg–Hg distance has the lowest total energy, ~ 0.2 eV/supercell lower than the other two. The first one is insulating with a band gap of 0.5 eV based on HSE06 calculations, while the other two are metallic. From the viewpoint of the importance of inducing superconductivity in this phase, it is unfortunate that the metallic structures have higher total energies and are therefore not expected to be stable.

Continuing to 50% doping (four Hg atoms), we consider initial configurations consisting of two pairs of Hg–Hg atoms based on the results of 25% doping. There are three different initial configurations resulting from replacing two Tl atoms by two Hg atoms in the first configuration of the 25% doping case; i.e., the other pair of Hg–Hg atoms are at (I) $(0, \frac{1}{2}, 0)$ and $(\frac{1}{2}, \frac{1}{2}, 0)$, (II) $(\frac{1}{2}, \frac{1}{2}, 0)$ and $(\frac{1}{2}, \frac{1}{2}, \frac{1}{2})$, and (III) $(\frac{1}{2}, \frac{1}{2}, \frac{1}{2})$ and $(0, \frac{1}{2}, \frac{1}{2})$. After relaxation, configuration I is

0.15 and 0.17 eV/supercell lower in total energy than configurations II and III, respectively. Configuration I is insulating with a band gap of ~ 1.0 eV based on HSE06, and the other two configurations are metallic, similar to the 25% doping case.

Now for 75% doping, there are six Hg atoms and two Tl atoms in the supercell. Here it is more convenient to consider the initial configuration of the two Tl atoms. Exactly the same as in the 25% doping case, the two Tl atoms have three different initial configurations, i.e., the two Tl atoms are at (A) (0, 0, 0) and (0, $1/2$, 0), (B) (0, 0, 0) and ($1/2$, $1/2$, 0), and (C) (0, 0, 0) and ($1/2$, $1/2$, $1/2$). In contrast to the 25% and 50% doping cases, all three configurations have similar total energies after relaxation, differing only by ~ 0.02 eV/supercell. Moreover, all three configurations are insulators with almost the same band gap of ~ 2.0 eV.

We further analyze the structure with the lowest total energy at each doping level. For the parent compound CsTlCl_3 , the Cl^- ions around Tl show breathing distortions, resulting in alternative expanded Tl^+Cl_6 and compressed $\text{Tl}^{3+}\text{Cl}_6$ octahedra. Thus, the $\text{Tl}^{1+/3+}$ ions are in mixed-valence states, whereas in CsHgCl_3 , the Hg^{2+} ions are in a single-valence state. A common theme of the structures of the doped $\text{Cs}(\text{Tl,Hg})\text{Cl}_3$ compounds found in the supercell calculations is that there are equal amounts of Tl^{3+} and Tl^+ ions with breathing-distorted Cl^- ions surrounding them, while the Cl^- ions around the Hg^{2+} ions form SOJT distorted octahedra, similar to the Jahn–Teller distortion in the parent compound CsAuCl_3 . In the 50% doping case, the material shows a quasi-layered structure with Hg atoms in the $z = 0$ plane and Tl atoms in the $z = 1/2$ plane. This structure could be difficult to form in practice. Experimentally, the 50% Hg-doped sample was not made successfully.

The evolution of the total density of states (DOS) from CsTlCl_3 to CsHgCl_3 is shown in Figure 7. With increasing Hg concentration, the main peak below the Fermi level, which consists mainly of Cl 3p states, moves toward the Fermi level, consistent with removing electrons from the materials (Hg has

one less electron than Tl). The band gap, computed by DFT-HSE06, first decreases from ~ 1.2 eV in CsTlCl_3 to ~ 0.5 eV in the 25% Hg-doped compound, increases to ~ 1.0 and ~ 2.0 eV in 50% and 75% doped compounds, respectively, and finally decreases again to ~ 0.6 eV in CsHgCl_3 . Small doping of Hg into CsTlCl_3 weakens the Cl breathing distortion centered at Tl atoms, which reduces the mixed valence of Tl atoms. As a result, the band gap decreases with small Hg doping, as shown in Figure 7. On the other hand, small Tl doping into CsHgCl_3 introduces large distortions of the Cl octahedra centered at both Hg and Tl atoms. The large distortions induced by Tl doping act to increase the band gap rapidly, as shown in Figure 7, where 25% Tl doping increases the band gap from ~ 0.6 eV in CsHgCl_3 to ~ 2.0 eV. On the basis of our study, Hg doping into CsTlCl_3 is unable to suppress the Cl breathing distortions and mixed valence of Tl; hence, it is unable to metallize the parent compound.

CONCLUSIONS

We have prepared the solid solution $\text{CsTl}_{1-x}\text{Hg}_x\text{Cl}_3$. $x = 0.1$ is tetragonal, $x = 0.2$ is cubic with space group $Fm\bar{3}m$ and two crystallographic positions for Tl^+ and Tl^{3+} , $x = 0.4$ and 0.5 cannot be prepared as single phases, and $x = 0.6$ and 0.8 are simple cubic perovskites, $Pm\bar{3}m$, and one single position for Tl^+ , Tl^{3+} , and Hg^{2+} . All of the samples are insulating, and there is no sign of superconductivity. By XAS, we observe an intermediate Tl valence state for the entire series, confirming the mixed valence of Tl^+ and Tl^{3+} . Raman spectroscopy shows the presence of active Tl–Cl–Tl stretching mode and the appearance of the Tl–Cl–Hg mode when the content of Hg increases. Theoretical calculations confirm that the ground states of all $\text{CsTl}_{1-x}\text{Hg}_x\text{Cl}_3$ phases are insulating and Hg doping cannot produce superconductivity.

ASSOCIATED CONTENT

Supporting Information

Crystallographic data and structure refinement of the samples using SCD. This material is available free of charge via the Internet at <http://pubs.acs.org>.

AUTHOR INFORMATION

Corresponding Author

*E-mail: martha@rutchem.rutgers.edu.

Present Addresses

‡M.R.: Nanoscience Center and Science Center, Niels Bohr Institute, University of Copenhagen, Copenhagen, Denmark.

||T.S.: Division of Solid State Physics, Department of Engineering Sciences, Uppsala University, Uppsala, Sweden.

Notes

The authors declare no competing financial interest.

ACKNOWLEDGMENTS

This work was supported by NSF Grant DMR-0966829. Z.Y. and G.K. were supported by the AFOSR-MURI program toward better and higher temperature superconductors. We gratefully acknowledge the high-resolution PXRD data collected at beamline X16C, NSLS, Brookhaven National Laboratory, supported by the U.S. Department of Energy, Office of Science, Office of Basic Energy Sciences, under Contract DE-AC02-98CH10886. The work at IOPCAS was supported by NSF and MOST research grants.

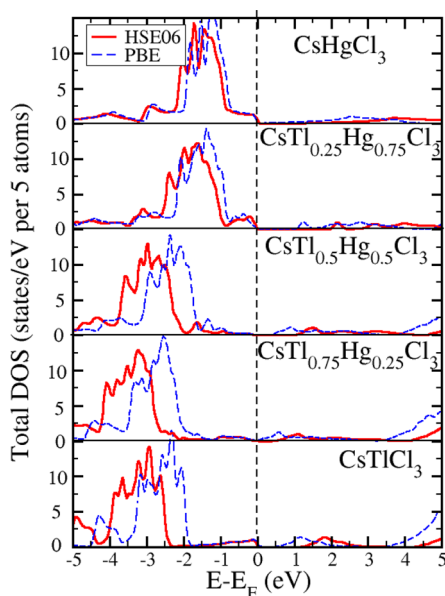


Figure 7. Total DOS per five atoms for CsTlCl_3 , $\text{CsTl}_{0.75}\text{Hg}_{0.25}\text{Cl}_3$, $\text{CsTl}_{0.5}\text{Hg}_{0.5}\text{Cl}_3$, $\text{CsTl}_{0.25}\text{Hg}_{0.75}\text{Cl}_3$, and CsHgCl_3 computed by DFT-PBE and DFT-HSE06.

■ REFERENCES

- (1) Cava, R.; Batlogg, B.; Krajewski, J.; Farrow, R.; Rupp, L.; White, A.; Short, K.; Peck, W.; Kometani, T. *Nature* **1988**, *332*, 814–816.
- (2) Yin, Z. P.; Kutepov, A.; Kotliar, G. *Phys. Rev. X* **2013**, *3*, 021011.
- (3) Baumert, B. *J. Supercond.* **1995**, *8*, 175–181.
- (4) Pei, S.; Jorgensen, J. D.; Dabrowski, B.; Hinks, D. G.; Richards, D. R.; Mitchell, A. W.; Newsam, J. M.; Sinha, S. K.; Vaknin, D.; Jacobson, A. *J. Phys. Rev. B* **1990**, *41*, 4126–4141.
- (5) Climent-Pascual, E.; Ni, N.; Jia, S.; Huang, Q.; Cava, R. *Phys. Rev. B* **2011**, *83*, 174512.
- (6) Kojima, N.; Hasegawa, M.; Kitagawa, H.; Kikegawa, T.; Shimomura, O. *J. Am. Chem. Soc.* **1994**, *116* (25), 11368–11374.
- (7) Kitagawa, H.; Sato, H.; Kojima, N.; Kikegawa, T.; Shimomura, O. *Solid State Commun.* **1991**, *78*, 989–995.
- (8) Kojima, N.; Kitagawa, H. *J. Chem. Soc., Dalton Trans.* **1994**, *3*, 327–331.
- (9) Wang, S.; Hirai, S.; Shapiro, M. C.; Riggs, S. C.; Geballe, T. H.; Mao, W. L.; Fisher, I. R. *Phys. Rev. B* **2013**, *87*, 054104.
- (10) Yin, Z. P.; Kotliar, G. *EPL* **2013**, *101*, 27002.
- (11) Schoop, L. M.; Muechler, L.; Felser, C.; Cava, R. *J. Inorg. Chem.* **2013**, *52*, 5479–5483.
- (12) Retuerto, M.; Emge, T.; Li, M. R.; Yin, Z. P.; Croft, M.; Ignatov, A.; Simonson, J.; Aronson, M.; Stephens, P.; Hadermann, J.; Pan, A.; Basov, D. N.; Kotliar, G.; Greenblatt, M. *Chem. Mater.* **2013**, *25*, 4071–4079.
- (13) Khan, Y.; Nahm, K.; Rosenberg, M.; Willner, H. *Phys. Status Solidi A* **1977**, *39*, 79–88.
- (14) TOPAS-Academic, version 5; Coelho Software: Brisbane, Australia, 2012.
- (15) SADABS; Bruker-AXS Inc.: Madison, WI, 2013.
- (16) Sheldrick, G. M. *Acta Crystallogr., Sect. A* **2008**, *64*, 112–122.
- (17) Petricek, V.; Dusek, M.; Palatinus, L. *JANA2006*; Institute of Physics: Prague, Czech Republic, 2006.
- (18) Huan, G.; Greaney, M.; Greenblatt, M.; Liang, G.; Croft, M. *Solid State Ionics* **1988**, *32–33*, 134–140.
- (19) Li, S.; Greenblatt, M.; Jeon, Y.; Chen, J.; Liang, G.; Croft, M. *Physica C* **1991**, *173*, 239–244.
- (20) Matsushita, N.; Ahsbans, H.; Hafner, S. S.; Kojima, N. *J. Solid State Chem.* **2007**, *180*, 1353–1360.
- (21) Bill, J.; Lerch, K.; Laqua, W. *Z. Anorg. Allg. Chem.* **1990**, *589*, 7–11.
- (22) Ferrari, A. *Gazz. Chim. Ital.* **1937**, *67*, 94–98.
- (23) Shannon, R. D. *Acta Crystallogr., Sect. A* **1976**, *32*, 751–767.
- (24) Li, S.; Greenblatt, M.; Jeon, Y.; Chen, J.; Croft, M. *Physica C* **1991**, *173*, 239–244.
- (25) Yang, T.; Abakumov, A.; Hadermann, J.; Van Tendeloo, G.; Nowik, I.; Stephens, P.; Hemberger, J.; Tsirlin, A.; Ramanujachary, K.; Lofland, S.; Croft, M.; Ignatov, A.; Sun, J.; Greenblatt, M. *Chem. Sci.* **2010**, *1*, 751–762.
- (26) Heald, S. M.; DiMarzio, D.; Croft, M.; Hegde, M. S.; Li, S.; Greenblatt, M. *Phys. Rev. B* **1989**, *40*, 8828–8833.
- (27) Glaser, T.; Hedman, B.; Hodgson, K.; Solomon, E. I. *Acc. Chem. Res.* **2000**, *33*, 859–868.
- (28) Kozimor, S. A.; Yang, P.; Batista, E. R.; Boland, K. S.; Burns, C. J.; Clark, D. L.; Conradson, S. D.; Martin, R. L.; Wilkerson, M. P.; Wolfsberg, L. E. *J. Am. Chem. Soc.* **2009**, *131*, 12125–12136.
- (29) Pakhomov, V. I.; Goryunov, A. V. *Zh. Neorg. Khim.* **1993**, *38*, 1501–1508.
- (30) Perdew, J. P.; Burke, K.; Ernzerhof, M. *Phys. Rev. Lett.* **1996**, *77*, 3865–3868.
- (31) Krukau, A. V.; Vydrov, O. A.; Izmaylov, A. F.; Scuseria, G. E. *J. Chem. Phys.* **2006**, *125*, 224106.
- (32) Kresse, G.; Furthmuller, J. *Comput. Mater. Sci.* **1996**, *6*, 15–50.